Structural Properties of Tin Doped Gadolinium Cerate as Novel Materials for Solid Oxide Fuel Cells

J. Maudood[1*], M. Hassan[2], M.S. Islam[1], I. B. Elius[1], A.K.M. Zakaria[4], K.A. Kabir[3] and S. Hossain[1*]

[1]*Institute of Nuclear Science and Technology, Atomic Energy Research Establishment GPO Box No 3787,Dhaka-1000, Bangladesh*

[2]*Chemistry Division, Atomic Energy Centre, Dhaka-1000, Bangladesh*

[3]*Department of Nuclear Engineering, University of Dhaka, Dhaka -1000, Bangladesh*

[4]*Bangladesh Atomic Energy Commission, Agargaon, Sher-e-Bangla Nagar, Dhaka-1207, Bangladesh*

Abstract

The novel polycrystalline of $Gd_{2-x}Sn_xCe_2O_7$ (x=0.1and 0.2) materials named as GSC1 and GSC2 were prepared by the conventional solid state sintering technique. The materials were sintered at 1300℃ for 10 hours in the air atmosphere. The X-ray diffraction (XRD) experiments were performed on both of the samples at room temperature with CuK_α radiation having wavelength λ=1.540562 Å and within the angular range of 2θ = 10° to 70°. The XRD experiments confirmed single phase cubic structure and space group was found to be Fm3m. The XRD data were analyzed using the Rietveld refinement method by computer code Full Prof suite. Thermo gravimetric analysis (TGA) experiment was done under the nitrogen atmosphere from room temperature to 800 ℃ in order to measure the thermal stability of the samples and the materials were found stable. To determine the grain growth and sizes, the SEM analysis was performed and it showed that Sn doping reduced the grain size. All of the studied properties show that the materials can be the potential candidate as the component material of SOFC.

Keywords: Perovskites, Solidstate sintering technique, X-ray diffraction, Thermo-gravimetric analysis, SEM

1. Introduction

To run the civilization, most of the required energy came from fossil fuels since the industrial revolution. Electrical energy can easily be produced from those sources but there is a massive drawback of using fossil fuel. A large amount of CO_2 has been released into the atmosphere in order to generate electrical energy from fossil fuels, which is 65% of the total greenhouse gases [1]. The use of renewable energy can reduce the emission of CO_2 by 70% by 2050 [2]. Considering this aspect, fuel cell technology can be an important technological advancement in the upcoming decade. But commercialization of fuel cells has been delayed due to the performance issues of their component materials. The main difficulty is that the electrolytes which have been discovered so far, do not have sufficient high proton conductivity. However, proton conducting perovskite type oxides have emerged as a promising class of materials for this purpose. In 1981, Iwahara et al. had investigated proton-conducting perovskites [3]. These proton conducting perovskites have been successfully used as electrolytes for numerous applications in fuel cells, sensors and batteries [4]. Due to their inherent advantages as electrolytes, solid oxide ceramics have been the subject of rigorous research. Compared to combustion based technologies, proton conducting perovskites have high efficiency [5]. Low emissions and fuel flexibility are also the advantages of these materials [6]. Moreover, in comparison to conventional oxygen ion conductors, proton conducting conductors exhibit a great advantage of possessing lower activation energies for proton transportation at reduced temperatures. Over the past few decades, most of the researches regarding proton conductors have been concentrated on acceptor doped $BaCeO_3$ oxides with a perovskite structure due to their preferable proton conductivity and a dense proton conducting electrolyte membrane. Unfortunately, doped $BaCeO_3$ oxides, in general, are susceptible to chemical degradation in the atmosphere containing water and carbon dioxide [5]. On the other hand, currently reasonable proton conduction was also observed in novel type ternary compounds, such as pyrochlore type oxides $La_2Zr_2O_7$, $Sm_2Sn_2O_7$ and fluorite type oxides $La_2Ce_2O_7$, $Nd_2Ce_2O_7$, $Gd_2Ce_2O_7$. Norby et al. have already confirmed that $La_2Ce_2O_7$ is a proton conductor at the operating range of proton conducting fuel cells, typically 600℃ [7]. Sun et al. reported that the proton conductivity of $La_2Ce_2O_7$ reached 6.68×10^{-5}scm^{-1} under wet air (3% H_2O) at 550℃ [8]. The observed peak power density of fuel cells based on $La_{1.95}Ca_{0.05}Ce_2O_{7-\delta}$ electrolytes achieved 259mWcm^{-2} at 700℃. The intrinsic oxygen vacancy enables $A_2B_2O_7$ type oxides to possess high electrical conductivity. Moreover, Liu et al. investigated the electrical properties of $Nd_2Ce_2O_7$ co-doped with Gd_2O_3 and ZrO_2 and the temperature dependency and the highest electrical conductivity is 1.62×10^{-2} scm^{-1} at 900℃ [9]. Recently, S. Cheng and L. E. Kalland systematically investigated the proton conduction behaviour of $Gd_2Ce_2O_7$ and $Nd_2Ce_2O_7$[10, 11]. It has been found that proton conduction in $Nd_2Ce_2O_7$ become predominant below 500℃ under wet conditions. Consequently, $Nd_2Ce_2O_7$ can be considered as a potential electrolyte candidate for proton conducting SOFCs [12]. However, the protonic conduction behaviour of $Gd_2Ce_2O_7$ and acceptor-doped $Gd_2Ce_2O_7$ oxides under wet hydrogen atmospheres is much less investigated. Therefore, it is really necessary to explore the improvement of proton

*Corresponding author: *jobair19@gmail.com*

conductivity and electrochemical performance of $Gd_2Ce_2O_7$ and acceptor-doped $Gd_2Ce_2O_7$ oxides. Sn-doping will enhance the electrical performance of $Gd_2Ce_2O_7$ electrolytes. Sn has been selected as the doping element in order to optimize the electrical conductivity and sintering activity of $Gd_2Ce_2O_7$ (GCO). In this study, powders having different $Gd_{2-x}Sn_xCe_2O_7$ compositions (x = 0.1 and 0.2) were synthesized via solid state reaction method. In this manuscript, some of the important structural features and their modification due to the Sn- substitution in gadolinium cerate were discussed in details.

2. Experimental

2.1 Sample Preparation

The samples $Gd_{2-x}Sn_xCe_2O_7$ named as GSC1 and GSC2 (x=0.1 and 0.2) were prepared by the conventional solid-state reaction method [13, 14]. The solid state method is referred to as the 'shake and bake' synthetic route. In this method, solid and metal oxide precursors are thoroughly mixed and then calcined to a high temperature to form the perovskite phase. This synthetic route is facile, however, it requires calcination at high temperature, typically in the vicinity of 900 ℃, leading to large crystal/particle size sand therefore a lower surface area for the perovskite phase [15, 16]. Moreover, metal evaporation from the sample can alter the desired stoichiometry of the perovskite and the high temperature calcination requires sophisticated equipment and immense energy.

The powder chemicals of Gd_2O_3, CeO_2 and SnO (the chemicals were from Sigma-Aldrich, purity were stated 99.90% in the containers) as initial ingredients were used in exact stoichiometric amounts. The ingredients were weighed individually using a precise digital microbalance and then thoroughly mixed in an agate mortar for 1 hour of each with a small amount of ethanol as a binding agent. The samples were then stirred for 30 minutes each on a magnetic stirrer and heated on a magnetic hotplate to ensure their homogeneity at a temperature of 80℃ until mixtures were well dried. The samples were then ground for 1 hour with two drops of PVA as a binder. After that, the pellets were made from the powder (2.5g of each) and were pressed under the hydraulic press with 3 tons of pressure. Then the pellets were heated inside a muffle furnace at 900℃ for 12 hours with both heating and cooling rate of 5℃/min for calcination. The calcined samples were reground and remixed in a mortar and pestle for 1 hour of each. Then pellets of a particular diameter (about 2.5 g/each) were pressed under the hydraulic press with 3 tons pressure. Then pre-sintering was done at 1200℃ for 18 hours followed by sintering at the temperature of 1300℃ for 10 hours. For both pre-sintering and sintering, the temperature of the muffle furnace was changed (raised/cooled) at a rate of 5℃/min.

2.2 Characterization of the materials

The X-ray powder diffraction technique was used to confirm the phase purity and to study the structure of the synthesized samples. The XRD studies of the samples were done by using the Ultima-IV X-ray diffract meter. The X-ray diffraction studies of all the materials (x=0.1 and 0.2) were performed at room temperature with CuK_α radiation (where λ=1.540562 Å) and at an angular range of 2θ =10° to 70°.

The thermogravimetric analysis (TGA) was done for both of the samples by using the Shimadzu Thermogravimetric Analyzer TGA 50 with control unit FC 40 and TA 50 WSI. The disc shaped pellets were sintered at 650ºC for 8 hours in a muffle furnace and the TGA measurements were done under the nitrogen atmosphere. The flow rate was 10 ml/min; alumina was used as a sample holder in the measurement process. The TGA measurements were performed from room temperature to 800 ºC. The initial weights of the samples GSC1 and GSC2 were 11.605 mg and 12.544 mg; respectively.

For themicrostructural, grain growth and the Sn doping effect on the samples of $Gd_{2-x}Sn_xCe_2O_7$, the SEM analysis was performed. The SEM pellets were prepared by using a uniaxial press and then sintered at 1300℃ for 10 hours in the air.

3. Results and Discussion

3.1 XRD and phase analysis

Figs. 1 and 2 show the Rietveld analyses of X-ray diffraction patterns of the sample GSC1 (x = 0.1) and GSC2 (x = 0.2); respectively and Fig. 3 shows the relative position of the XRD peaks of two samples. From the XRD pattern of sample GSC1, the Bragg peaks were observed at the 2θ angular positions 28.473°(111), 32.992°(200), 47.368°(220), 56.189°(311), 58.92°(222) and 69.24°(400) and for the sample GSC2 the characteristic peaks were located at 28.597°(111), 33.082°(200), 47.498°(220), 56.273°(311), 59.10°(222) and 69.389°(400) angular positions. Initially, the indexing of the XRD data of the samples was done with the software *'Chekcell'* and also visually referenced the perovskites having similar symmetry and structure [17, 18]. Both the XRD patterns of the samples confirmed single phase cubic structure with the space group Fm3m of (Space group no.: 225).Then the 'Full Prof Suite' software was used for the Rietveld refinement of the diffraction data [19, 20]. It has been observed that, due to the increment of Sn concentration in $Gd_{2-x}Sn_xCe_2O_7$, the characteristic XRD peaks of GSC2 tend to shift towards higher angles. This shifting has been occurred because of the substitution of a relatively smaller ionic radius of tin Sn^{4+} (ionic radius=0.69 Å, coordination number (CN) 6) in place of a larger ionic radius of gadolinium Gd^{3+} (ionic radius=0.935Å in the same CN) ion.

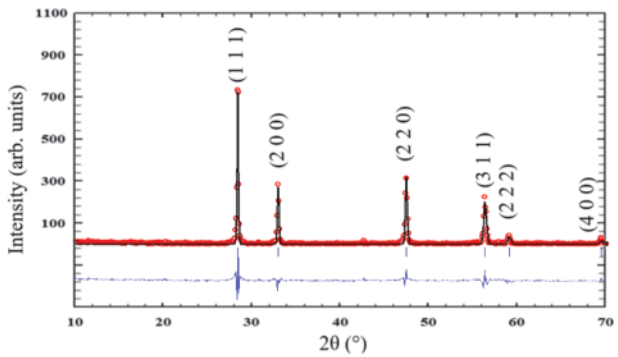

Fig. 1: Rietveld analysis of the XRD data for the sample $Gd_{2-x}Sn_xCe_2O_7$ (x=0.1)

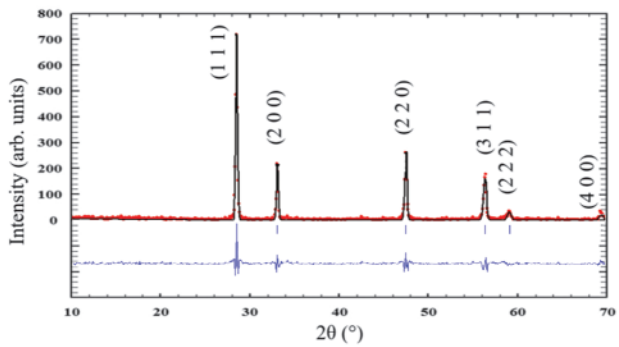

Fig. 2: Rietveld analysis of the XRD data for the sample $Gd_{2-x}Sn_xCe_2O_7$ (x=0.2)

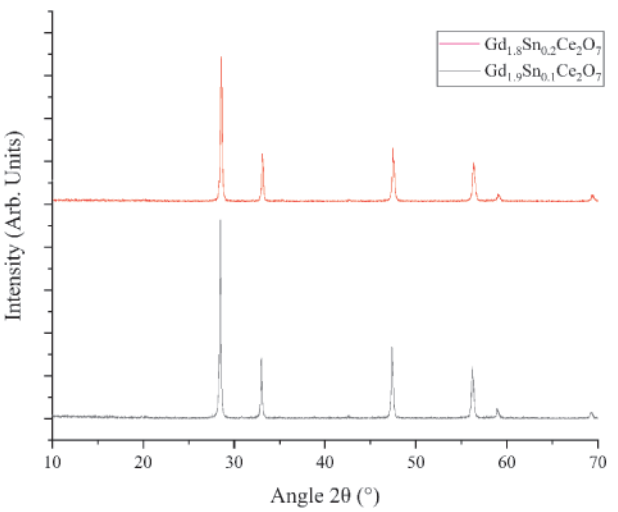

Fig. 3: XRD patterns for the sample $Gd_{1.9}Sn_{0.1}Ce_2O_7$ and$Gd_{1.8}Sn_{0.2}Ce_2O_7$

Figure 4 shows (a) polyhedral shape and (b) ball and stick diagram of GSC1 material after Rietveld refinement of the XRD data. It is found that the Ce atom is in the center of the crystal and Gd/Sn atom is in the corner of the crystal. Oxygen atoms are positioned at the edge of the crystal structure which shows the double perovskite structure.

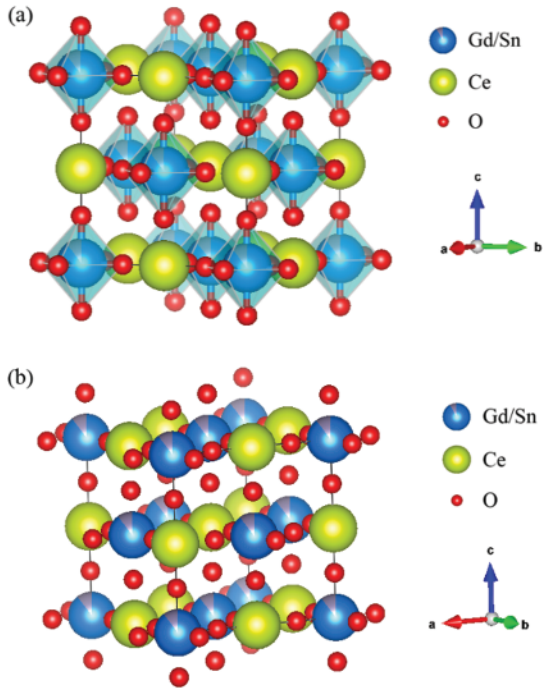

Fig. 4: (a) Polyhedral shape, (b) Ball and stick diagram of GSC1 material after refinement

The site occupied by different ions for $Gd_{2-x}Sn_xCe_2O_7$ with x = 0.1 and x = 0.2 from the Rietveld refinement with Fm3m space group is presented in Table 1.

Table 1: Site occupied by different ions for $Gd_{2-x}Sn_xCe_2O_7$ with x=0.1 and x=0.2 from the Rietveld refinement with Fm^3m space group

Ion	Site	Symmetry	Coordinates			Occupancy	
			X	Y	Z	x = 0.1	x = 0.2
Gd^{3+}(A)	4a	Fm^3m	0	0	0	0.00383	0.43681
Sn^{4+}(B)	4a	Fm^3m	0	0	0	0.74476	0.05137
Ce^{3+}(A)	4b	Fm^3m	0	0	0	0.27071	0.50137

From the indexing of XRD data, lattice parameters for both of the samples have been calculated and shown in Table 2. For GSC1 and GSC2, the lattice constants are found to be 5.4161Å and 5.4012Å; respectively. The lattice parameters decreased as the Sn doping concentration increased. As a result, the unit cell volume for GSC2 is also reduced to 157.4640Å^3 from 158.8793Å^3. The oxygen parameter U is also decreased as Sn doping concentration is increased by a small amount.

Table 2 also demonstrates the different R factors of the Rietveld refinement process. The criteria of a fit can be quantified with several minimized residual (R) values. The most common of these R values are the minimum achievable pattern residual, R_p and the weighted pattern residual, R_{wp}. From a purely mathematical point of view, R_{wp} is more meaningful than R_p. If the value of R_{wp} is

minimized, then it reflects the progress of the refinement. The goodness of fit (χ^2) of the materials GSC1 and GSC2 are found to be 2.36 and 2.25; respectively.

The variation of inter-atomic distances between the ions in sample GSC1 and GSC2 has also been shown in this table. The bond lengths between the different ions in the samples GSC1 and GSC2 have been calculated by using the 'BondStr' code based on CrysFML (Crystallographic Fortran 95 Modules Library) [21]. For GSC1, the average inter-atomic distance between Gd-O, Sn-O and Ce-O is 2.3453Å and for the GSC2 sample, the average inter-atomic distance is 2.3383Å. So the average bond length gets decreased as the doping concentration of Sn is increased. This is because the lattice parameter gets reduced to 5.4012 Å in GSC2 from 5.4161 Å in sample GSC1. As a result, the average bond length between the ions is also gets reduced by some small amount.

Table 2: Structural parameters, R-factors and inter atomic distances for $Gd_{2-x}Sn_xCe_2O_7$ with x=0.1 and x=0.2 from the Rietveld refinement

Parameters	$Gd_{2-x}Sn_xCe_2O_7$ x = 0.1 (GSC1)	$Gd_{2-x}Sn_xCe_2O_7$ x = 0.2 (GSC2)
Lattice Parameter, a (Å)	5.416161	5.401217
Oxygen Parameter, U	2.485532	1.531525
Volume, V (Å^3)	158.8793	157.4640
Profile Factor, R_P	55.40	49.9
Weighted Profile Factor, R_{WP}	68.00	64.9
Expected Weighted Profile Factor, R_E	29.37	28.20
Crystallographic Factor, R_F	19.19	14.18
Bragg's R factor, R_B	26.79	20.59
Goodness of fit, χ^2	2.36	2.25
Gd-O(Å)	2.3453	2.3383
Sn-O(Å)	2.3453	2.3383
Ce-O(Å)	2.3453	2.3383

In Full Profsuite software, the crystallographic structure factor $F_{\mathbf{h}}$ is calculated using the following formula:

$$F_{\boldsymbol{h}} = \sum_{j=1}^{n} O_j f_j(\boldsymbol{h}) \exp(-B_j|h| /4) \sum_{s=1}^{m} T_{js}(\boldsymbol{h}) \exp\{2\pi i(\boldsymbol{h}^T S_s \boldsymbol{r}_j + \boldsymbol{h}^T \boldsymbol{t}_s)\} \quad (1)$$

where n is the number of atoms in the asymmetric unit, m is the number of the reduced set of symmetry operators (centring lattice translations and inversion center operators removed). O_j is the occupation factor, $f_j(\boldsymbol{h})$ is the scattering length (in electron units for X-rays, in 10^{-12} cm for neutrons), B_j is the isotropic temperature parameter given is Å^2, and $\boldsymbol{r}_j$ is the position vector of atom j. The symmetry operator $\{S_s|t_s\} = \{S|t\}_s$ is applied to the scattering vector h (treated here as a column matrix) instead of the position vector. h^T is a row matrix with elements (hkl). $T_{js}(h)$ is the temperature factor.

On the other hand, in XRD experiments, waves get diffracted from scattering planes h, k and l (also known as Miller indices h[=(h k l)]). In this case, the diffracted waves can be described by structure factors, F_{hkl}. The electron density as a function of position x, y, z is the Fourier transform of the structure factors. A definition of the structure factor in terms of electron density distribution function is given in equation (2).

$$F_{hkl} = V \int_0^1 \int_0^1 \int_0^1 \rho(x,y,z) e^{2\pi i(hx+ky+lz)} dxdydz \quad (2)$$

where, ρ (x, y, z) is the electron density at the point (x, y, z).

The set of structure factors F_{hkl} is the Fourier transform of the electron density function. So ρ(x, y, z) in equation (2) can be expressed in terms of the structure factors F_{hkl} as shown in equation (3).

$$\rho(x,y,z) = \left(\frac{1}{V}\right) \sum_h \sum_k \sum_l F_{hkl} e^{-2\pi i(hz+ky+lz)} \quad (3)$$

The numerical computation of ρ(x, y, z) using F_{hkl} data is called a Fourier synthesis. ρ(x, y, z) is usually plotted as a three-dimensional contour map, called an electron density map.

The electron density mapping was calculated from XRD data by using the G Fourier program of the FullProf suite software. The electron density map of GSC1 and GSC2 are shown in figs. 5 and 6, respectively. In the figures, the charge of the scale has been inverted because the charge of the electron is considered as a unit. It can be seen from the figures that when the concentration of Sn is increased, the yellow region is also increased. This is because the electron affinity of Sn (1.112 eV) is greater than that of Gd (0.137 eV) [22, 23].

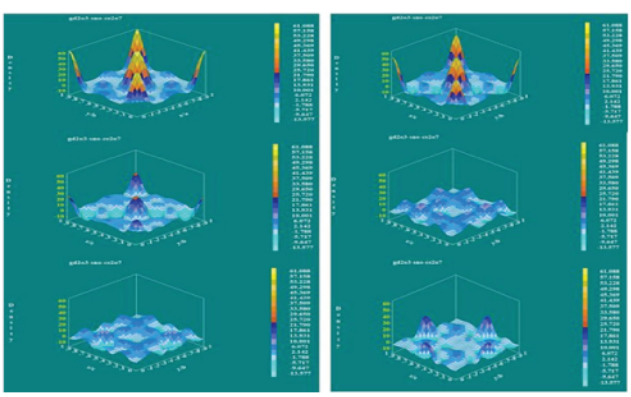

Fig. 5: Electron density map for GSC1

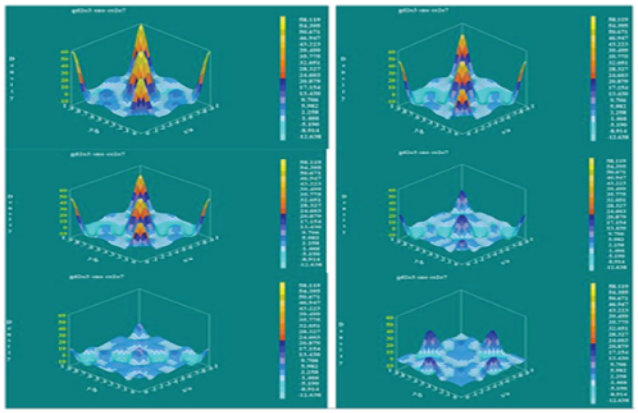

Fig. 6: Electron density map for GSC2

3.2 Thermogravimetric analysis

The results obtained from thermogravimetric analysis (TGA) are illustrated in figure 7. The chemical stability of the samples has been measured from TGA data analysis. The mass of GSC1 and GSC2 have been reduced by 0% and 0.64%; respectively. Initially, the weight of the GSC1 sample was 11.605 mg at 25℃ and throughout the measurement time, there was no significant change in mass. The percentage of mass loss increased by a small amount with an increase in Sn doping concentration. For the sample GSC2, the initial weight was 12.544 mg at 25℃ and at 378.11℃, the percentage of weight loss was found to be 0.04% and finally, it was observed that at 800℃ it was reduced by 0.64%. The observation was seen as due to a possible ordering of Stannum atom in the structure of sample GSC2, due to the dopant or vacancy ordering and there could be possible trapping of water in the structure that may have been retained in the sample.

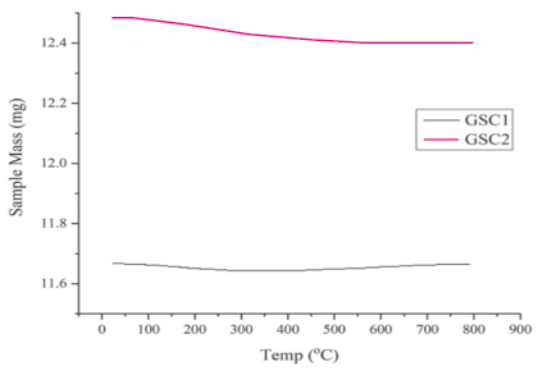

Fig. 7: TGA Curve for GSC1 and GSC2

The TGA results show the increase in Sn dopant leads to an increase in the number of vacancies and it is found that the GSC1 sample is thermally more stable than GSC2 under the N_2 atmosphere at the operating temperature ranging from room temperature to 800℃.

3.3 Scanning electron microscopy

Fig. 8 (a-c) show the SEM images of GSC1 at magnification level 2000, 4500 and 10000; respectively and Figs. 9 (a-c) show SEM images of GSC2 at magnification level 2000, 5000 and 10000; respectively. From these images, it can be found that the average grain sizes of $Gd_{2-x}Sn_xCe_2O_7$ pellets have remarkably improved with a small amount of Sn doping. The grain size for the GSC1 pellets is 2.266μm and for GSC2 pellets it has been found to be 1.649μm. Average grain sizes of GSC1 and GSC2 at different magnification level is shown in Table 3. From the SEM images of GSC1, a detectable amount of porosity can be seen but as the Sn concentration is increased from 0.1 to 0.2 the amount of porosity is decreasing and the GSC2 sample is getting denser than GSC1.

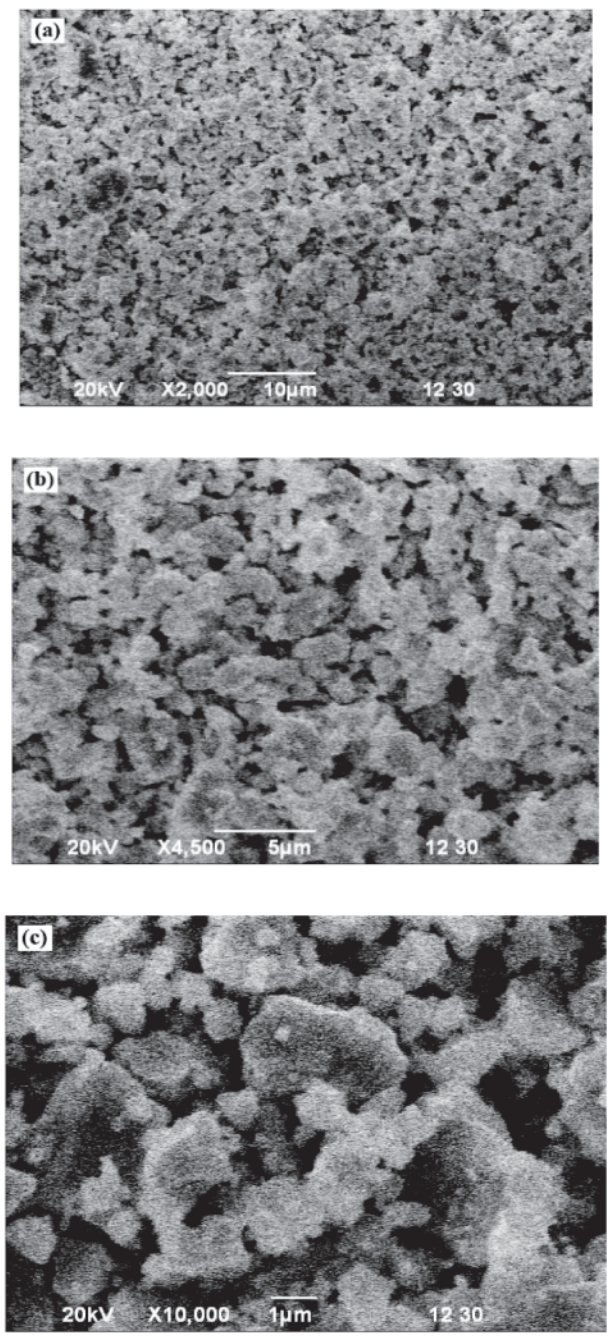

Fig. 8: SEM image of GSC1. In (a), (b) and (c) the magnification level is 2000, 4500 and 10000 respectively

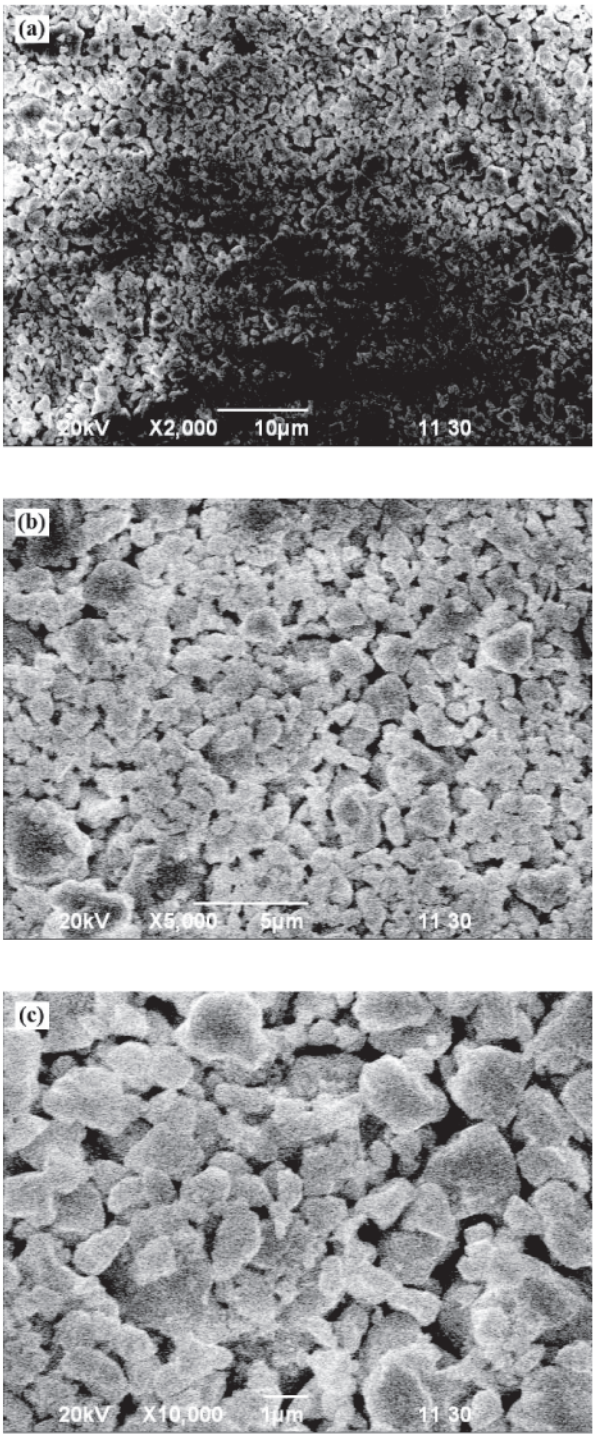

Fig. 9: SEM image of GSC2. In (a), (b) and (c) the magnification level is 2000, 5000 and 10000; respectively

It is expected that the electrolyte material should be highly dense so that its transport properties are improved. Grain growth and densification are strongly dependent on the sintering temperature and sintering additive. From the microstructure analysis, it can be found that Sn doping is very significant for grain growth and densification.

Table 3: Average grain size of $Gd_{2-x}Sn_xCe_2O_7$ (x=0.1 and 0.2) at different magnification

Composition	Average Grain Size at Magnification			
	×2000	×4500	×5000	×10000
GSC1 (x=0.1)	2.052	2.198	-	2.266
GSC2 (x=0.2)	1.570	-	1.647	1.649

4. Conclusion

The perovskites samples of $Gd_{2-x}Sn_xCe_2O_7$ (where x=0.1 and 0.2, named as GSC1 and GSC2) were synthesized using the solid state sintering method and the sintering was done at 1300℃ for 10 hours. In the Rietveld analysis of the XRD data, it was confirmed that these samples possess single phase cubic structure with a space group of Fm3m. It is found that the lattice parameters, unit cell volume and oxygen parameters had decreased with the increment of the doping concentration of Sn and it was evident that with the increment of Sn concentration, the average bond length has decreased. From the TGA analysis, it was found that the samples exhibited no significant mass loss and are stable. The GSC1 is more thermally stable than the GSC2 sample. From the SEM analysis, it can be seen that average grain size improved with Sn doping. When the Sn doping was increased by a small amount, porosity was decreased and the sample was getting denser. From the studied properties of the materials, it can be said that the materials can be the potential candidate as the component material of SOFC.

References

1. Intergovernmental Panel on Climate Change, Climate Change 2014 Mitigation of Climate Change Cambridge: Cambridge University Press (2015).
2. I. Energy Agency and I. Renewable Energy Agency, Perspectives for the Energy Transition: Investment Needs for a Low-Carbon Energy System (2017).
3. H. Iwahara, Y. Asakura, K. Katahira and M. Tanaka, Prospect of hydrogen technology using proton-conducting ceramics, Solid State Ionics, **168(3-4)**, 299-310 (2004).
4. S. Hossain, A.M. Abdalla, N. Radenahmad, A.K.M. Zakaria, J.H. Zaini, S.M.H. Rahman, S.G. Eriksson, J.T.S. Irvine and A.K. Azad, Highly dense and chemically stable proton conducting electrolyte sintered at 1200 °C, Int. J. Hydrogen Energy, **43(2)**, 894-907 (2018).
5. S. Hossain, A.M. Abdalla, S.N.B. Jamain, J.H. Zaini and A. K. Azad, A review on proton conducting electrolytes for clean energy and intermediate temperature-solid oxide fuel cells, Renew. Sustain. Energy Rev., **79 (September 2016)**, 750-764 (2017).
6. L. Malavasi, C.A.J. Fisher and M.S. Islam, Oxide-ion and proton conducting electrolyte materials for clean energy applications: Structural and mechanistic features, Chem. Soc. Rev., **39(11)**, 4370-4387 (2010).

7. V. Besikiotis, C.S. Knee, I. Ahmed, R. Haugsrud and T. Norby, Crystal structure, hydration and ionic conductivity of the inherently oxygen-deficient $La_2Ce_2O_7$, Solid State Ionics, **228**, 1–7 (2012).
8. W. Sun, S. Fang, L. Yan and W. Liu, Investigation on proton conductivity of $La_2Ce_2O_7$ in wet atmosphere: Dependence on water vapor partial pressure, Fuel Cells, **12(3)**, 457-463 (2012).
9. Z.-G. Liu, J.-H. Ouyang and K.-N. Sun, Electrical Conductivity Improvement of $Nd_2Ce_2O_7$ Ceramic Co-doped with Gd_2O_3 and ZrO_2, Fuel Cells, **11(2)**, 153-157 (2011).
10. S. Cheng, Defects and transport in fluorite related materials $Nd_2Ce_2O_7$ and $Gd_2Ce_2O_7$, University of Oslo (2012).
11. L. E. Kalland, A. Løken, T. S. Bjørheim, R. Haugsrud and T. Norby, Structure, hydration, and proton conductivity in 50% La and Nd doped CeO_2 - $La_2Ce_2O_7$ and $Nd_2Ce_2O_7$ and their solid solutions, Solid State Ionics, **354 (June)**, 115401 (2020).
12. M. Malathi, K. Sreenu, G. Ravi, P.V. Kumar, C. Sudhakar Reddy, R. Guje, R. Velchuri and M. Vithal, Low temperature synthesis of fluorite-type Ce-based oxides of composition $Ln_2Ce_2O_7$ (Ln = Pr, Nd and Eu): photodegradation and Luminescence studies, J. Chem. Sci., **129(8)**, 1193-1203 (2017).
13. A.M. Abdalla, S. Hossain, P.M.I. Petra, C.D. Savaniu, J.T. S. Irvine and A.K. Azad, Novel layered perovskite $SmBaMn_2O_{5+\delta}$ for SOFCs anode material, Mater. Lett., **204**, 129-132 (2017).
14. S. Tao and J.T.S. Irvine, Conductivity studies of dense yttrium-doped $BaZrO_3$ sintered at 1325°C, J. Solid State Chem., **180(12)**, 3493-3503 (2007).
15. A. Ecija, K. Vidal, A. Larraaga, L. Ortega-San-Martn, and M. Isabel, Synthetic Methods for Perovskite Materials; Structure and Morphology, Adv. Cryst. Process, (2012).
16. F. S. Galasso, Structure, Properties and Preparation of Perovskite-Type Compounds: International Series of Monographs in Solid State Physics, **5**, (2013).
17. I. B. Elius, B. M. Asif, J. Maudood, T. K. Datta, A. K. M. Zakaria, S. Hossain, M. S. Aktar and I. Kamal, Synthesis and Characterization of Strontium Doped Barium Titanates using Neutron Diffraction Technique, Nucl. Sci. Appl., **28(1)**, 57-62, (2019).
18. S. Hossain, A.M. Abdalla, J.H. Zaini, C.D. Savaniu, J.T.S. Irvine and A.K. Azad, Highly dense and novel proton conducting materials for SOFC electrolyte, Int. J. Hydrogen Energy, **42(44)**, 27308–27322 (2017).
19. R. Carvajal, Tutorial on Magnetic Structure Determination and Refinement using Neutron Powder Diffraction and FullProf (2014).
20. A. M. Abdalla, S. Hossain, J. Zhou, P. M. I. Petra, S. Erikson, C. D. Savaniu, J. T. S. Irvine and A. K. Azad, $NdBaMn_2O_{5+\delta}$ layered perovskite as an active cathode material for solid oxide fuel cells, Ceram. Int., **43(17)**, 15932-15938, (2017).
21. N. A. Katcho, J. Carrete, M. Reynaud, G. Rousse, M. Casas-Cabanas, N. Mingo, J. Rodríguez-Carvajal and J. Carrasco, An investigation of the structural properties of Li and Na fast ion conductors using high-throughput bond-valence calculations and machine learning, J. Appl. Crystallogr., **52(1)**, 148-157 (2019).
22. M. Vandevraye, C. Drag and C. Blondel, Electron affinity of tin measured by photodetachment microscopy, J. Phys. B At. Mol. Opt. Phys., **46(12)**, 125002 (2013).
23. Z. Felfli, A.Z. Msezane and D. Sokolovski, Resonances in low-energy electron elastic cross sections for lanthanide atoms, Phys. Rev. A, **79(1)**, 12714 (2009).